ADVANCED ENERGY MATERIALS
www.advenergymat.de

Reducing Saturation-Current Density to Realize High-Efficiency Low-Bandgap Mixed Tin–Lead Halide Perovskite Solar Cells

Chongwen Li, Zhaoning Song, Dewei Zhao, Chuanxiao Xiao, Biwas Subedi, Niraj Shrestha, Maxwell M. Junda, Changlei Wang, Chun-Sheng Jiang, Mowafak Al-Jassim, Randy J. Ellingson, Nikolas J. Podraza, Kai Zhu, and Yanfa Yan**

The unsatisfactory performance of low-bandgap mixed tin (Sn)–lead (Pb) halide perovskite subcells has been one of the major obstacles hindering the progress of the power conversion efficiencies (PCEs) of all-perovskite tandem solar cells. By analyzing dark-current density and distribution, it is identified that charge recombination at grain boundaries is a key factor limiting the performance of low-bandgap mixed Sn–Pb halide perovskite subcells. It is further found that bromine (Br) incorporation can effectively passivate grain boundaries and lower the dark current density by two–three orders of magnitude. By optimizing the Br concentration, low-bandgap (1.272 eV) mixed Sn–Pb halide perovskite solar cells are fabricated with open-circuit voltage deficits as low as 0.384 V and fill factors as high as 75%. The best-performing device demonstrates a PCE of >19%. The results suggest an important direction for improving the performance of low-bandgap mixed Sn–Pb halide perovskite solar cells.

Organic–inorganic metal halide perovskite solar cells (PSCs) have been extensively investigated as a promising thin film photovoltaic technology due to their high efficiencies, low material cost, and low-temperature solution processability.[1–6] The record power conversion efficiency (PCE) of single-junction cells has rapidly increased to a certified 23.3%.[2,5,7–9] The bandgap tunability and low-temperature processability make metal halide perovskites ideal candidates to realize all-perovskite thin-film tandem solar cells, which hold the promise to obtain ultrahigh efficiency and be fabricated at low cost on light-weight and flexible substrates.[10–13]

C. Li, Dr. Z. Song, Dr. D. Zhao, B. Subedi, N. Shrestha, Dr. M. M. Junda, C. Wang, Prof. R. J. Ellingson, Prof. N. J. Podraza, Prof. Y. Yan
Department of Physics and Astronomy and Wright Center for Photovoltaics Innovation and Commercialization
The University of Toledo
2801 W. Bancroft Street, Toledo, OH 43606, USA
E-mail: dewei_zhao@hotmail.com; yanfa.yan@utoledo.edu
Dr. C. Xiao, Dr. C.-S. Jiang, Dr. M. Al-Jassim, Dr. K. Zhu
National Renewable Energy Laboratory
15013 Denver West Parkway, Golden, CO 80401, USA
The ORCID identification number(s) for the author(s) of this article can be found under https://doi.org/10.1002/aenm.201803135.

DOI: 10.1002/aenm.201803135

For a two-terminal monolithic tandem solar cell, the open-circuit voltage (V_{OC}) is the sum of the V_{OC}s of the wide-bandgap and low-bandgap subcells while the short-circuit current density (J_{SC}) is limited by the lower J_{SC} of the subcells. Therefore, achieving high V_{OC}s for both subcells while maintaining a sufficiently high J_{SC} for current matching is critical for realizing high-efficiency two-terminal tandem solar cells. For all-perovskite tandem solar cells, the commonly used wide-bandgap (wide-E_g) subcell (≈1.7–1.9 eV) is based on $FA_{1-x}Cs_xPb(I_{1-y}Br_y)_3$ perovskite absorbers ($0 < x, y < 1$) (FA = formamidinium, Cs = cesium, I = iodide, Br = bromide), whereas the low-bandgap (low-E_g) (≈1.1–1.3 eV) subcell is based on tin (Sn)–lead (Pb) halide perovskite absorbers.[12–15]

While wide-E_g PSCs have achieved remarkable improvement in performance via composition tuning/engineering, annealing engineering, and interface engineering,[16–19] the performances of low-E_g PSCs reported in the literature are still not satisfactory. Significant efforts have been made to improve the performance of low-E_g PSCs.[6,11,20–27] Kanatzidis and co-workers have first reported the bowing effect in mixed Sn–Pb perovskites, revealing the opportunity of bandgap tuning via compositional engineering.[20] McGehee and co–workers have studied the effect of lattice contraction and octahedral tilting on bandgap tuning in low-E_g mixed Sn–Pb perovskites.[21] Hayase and co-workers have introduced an n-type "spike structure" interface to improve the charge flow at the interface of the absorber and electron transport layer (ETL).[28] Our group has boosted the efficiency to a certified value of 17% for relatively thick low-E_g (1.25 eV) PSCs, beneficial for all-perovskite tandem solar cells.[6,23,24,29] Recently, Jen and co-workers have incorporated 20% Br into low-E_g $MASn_{0.5}Pb_{0.5}I_3$ (MA = methylammonium) perovskite to obtain an optimal bandgap (1.35 eV) for single-junction PSC applications, and a V_{OC} of 0.9 V was obtained.[26] However, the relatively large E_g limits its potential for applications as the low-E_g bottom subcells for tandem devices.[13] So far, many reported low-E_g mixed Sn–Pb PSCs show relatively large V_{OC} deficits (E_g/q-V_{OC}, where q is the unit charge) and/or low fill factors

© 2018 WILEY-VCH Verlag GmbH & Co. KGaA, Weinheim

(FFs), which are the key limitations for recently reported two-terminal all-perovskite tandem solar cells.[12–14]

Current density–voltage (J–V) characteristic of a solar cell is typically governed by the diode law. Based on the diode equation, the V_{OC} of a single-junction solar cell can be described as $V_{OC} = \frac{nkT}{q}\ln\left(\frac{J_{SC}}{J_0}+1\right)$, where n is the ideality factor, k is Boltzmann constant, T is the temperature, and J_{SC} and J_0 are the photogenerated and dark saturation current densities, respectively. The equation indicates the dependence of V_{OC} on both J_{SC} and J_0. For a given absorber material thickness under one-sun illumination, J_{SC} typically has a small variation; however, J_0, which is determined by the charge recombination in the cell, may vary by several orders of magnitude, and therefore can be used as an indicator of the performance of a solar cell. Additionally, V_{OC} is also proportional to n, which is also related to the charge recombination in the cell. A solar cell with a high n value typically correlates with a high J_0. Therefore, to realize a high-efficiency solar cell with a large V_{OC}, a low J_0 is highly necessary.[30]

Here, we evaluate the performance of low-E_g mixed Sn–Pb PSCs by analyzing J_0 and dark current distributions. We found that low-E_g mixed Sn–Pb PSCs have J_0 that is around five orders of magnitude higher than that measured in PSCs with medium- or wide-bandgap perovskite absorbers. Conductive atomic force microscopy (c-AFM) results revealed that the high J_0 is mainly due to contributions by regions near grain boundaries (GBs). We further found that Br incorporation can effectively passivate GBs and lower the J_0 by 2 or 3 orders of magnitude. However, Br incorporation can also reduce the majority carrier density and increase Urbach energy (E_u), which have negative impacts on device performance. Additionally, Br incorporation increases the bandgap, which is not preferable for applications in all-perovskite tandem PSCs. By optimizing the Br concentration, we successfully fabricated low-E_g (1.272 eV) mixed Sn–Pb PSCs with V_{OC} deficits as low as 0.384 V without obvious reduction in J_{SC}. The best-performing device achieved a PCE of >19%. Our work suggests an important direction for further improving the performance of low-E_g mixed Sn–Pb halide PSCs.

Figure 1a compares the dark J–V curves of medium-E_g $FA_{0.3}MA_{0.7}PbI_3$[31–33] and low-E_g $(FASnI_3)_{0.6}(MAPbI_3)_{0.4}$ PSCs with the p–i–n structure, i.e., glass/indium tin oxide (ITO)/hole transport layer (HTL)/perovskite/fullerene (C_{60})/2,9-dimethyl-4,7-diphenyl-1,10-phenanthroline (BCP)/Ag.[23,24,34] poly(bis(4-phenyl)(2,4,6-trimethylphenyl)amine) (PTAA) and poly(2,3-dihydrothieno-1,4-dioxin)-poly(styrenesulfonate) (PEDOT:PSS) are used as HTLs for medium E_g and low-E_g PSCs, respectively. J_0 can be determined by the intercept at zero voltage of the linear regression from the semi-logarithmic J–V plot in the region close to the diode turn-on voltage. Generally, the bandgap dependency of J_0 can be described as $J_0 \propto \exp(-E_g/nkT)$, showing that J_0 depends on E_g and n. As shown in Figure S1 (Supporting Information), for a medium-E_g (1.6 eV) $FA_{0.3}MA_{0.7}PbI_3$ PSC, J_0 and n are estimated to be 2.7×10^{-11} mA cm^{-2} and 1.35; whereas, J_0 and n of the low-E_g (1.25 eV) PSC are 10^{-5} mA cm^{-2} and 1.65. Such high J_0 and n values of the low-E_g PSC indicate a high leakage current density and significant carrier recombination outside the depletion region, which limit the V_{OC}, FF, and therefore, PCE of low-E_g PSCs.

To identify the root of the high J_0 values, we have conducted c-AFM analysis of unfinished low-E_g PSCs without ETL and Ag layers. The c-AFM image (**Figure 2**a) clearly shows that local current density is much higher in vicinity of GBs than in grain interiors (GIs). In the c-AFM setup, the local current is determined by the sum of series-connected resistances of the local HTL/perovskite junction, the perovskite film, and probe/perovskite contact. Because the large equivalent resistance of the junction should dominate the measured resistance and the current route should not significantly spread from the local probe/perovskite contact due to the thin thickness of perovskite film (less than 1 µm), the local current density measured from c-AFM qualitatively reflects the variation of J_0 in the device. The low current density right at the GBs could be the result of reduced contact area of the probe due to possible surface valleys at GBs.

The results suggest that the high J_0 values of our low-E_g PSCs are mainly caused by high leakage current from GBs, which are expected to have much higher defect densities than GIs. Therefore, to improve device performance, the J_0 near at GBs must be significantly suppressed. The J_0–E_g relationship suggests that increasing the E_g and passivating the defects (which decreases n) are the appropriate methods to reduce J_0. It is known that Br and chloride (Cl) incorporation in iodide-based perovskites leads to segregation of Br and Cl, which passivates GBs.[23,24] The segregation of Br or Cl is also expected to increase

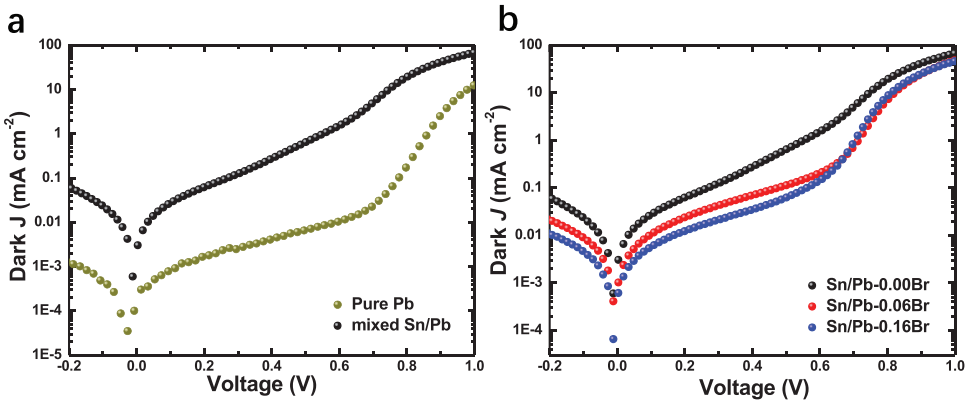

Figure 1. a) Dark J–V curves of medium-E_g pure Pb and low-E_g mixed Sn-Pb PSCs. b) Dark J–V curves of low-E_g mixed Sn–Pb PSCs with Br concentrations of 0, 0.06, and 0.16.

© 2018 WILEY-VCH Verlag GmbH & Co. KGaA, Weinheim

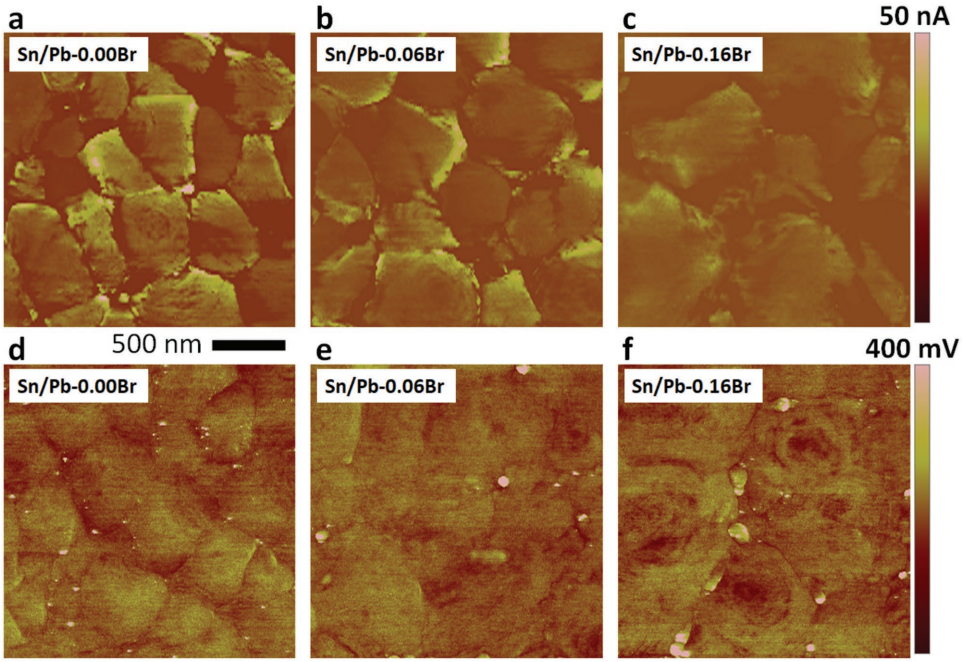

Figure 2. a–c) AFM and d–f) KPFM images of unfinished low-E_g PSCs with different Br concentrations: Sn/Pb-0.00Br, Sn/Pb-0.06Br, and Sn/Pb-0.16Br.

the bandgap of the GB regions. Therefore, Br and Cl incorporation could reduce the J_0 at GBs in low-E_g PSCs. We introduced Br incorporation in our low-E_g mixed Sn–Pb perovskites by mixing stoichiometric molar ratio of $(FASnI_3)_{0.6}(MAPbI_3)_{0.4-x}$ and $(MAPbBr_3)_x$ ($0 < x < 0.4$) to form a $(FASnI_3)_{0.6}(MAPbI_3)_{0.4-x}(MAPbBr_3)_x$ precursor ($x = 0$, 0.04, 0.06, 0.08, and 0.16), in which the molar ratio of Sn to Pb is kept identical at 0.6:0.4. Detailed evolution and dynamic processes of the crystallization of Br doped low-E_g perovskite films can be found in Figure S2 (Supporting Information). As expected, when Br content in $(FASnI_3)_{0.6}(MAPbI_3)_{0.4-x}(MAPbBr_3)_x$ perovskites increased from 0 (referred to as Sn/Pb-0.00Br) to 0.06 (Sn/Pb-0.06Br) and to 0.16 (Sn/Pb-0.16Br), J_0 decreased from 10^{-5} to 10^{-9} and to 10^{-10} mA cm^{-2}, respectively (Figure 1b; Figure S1, Supporting Information). Additionally, both shunt conductance and series resistance decreased with the addition of Br incorporation; n decreased from 1.65 to 1.34 and to 1.23 when Br content was increased from 0 to 0.06 and to 0.16, respectively (**Table 1**; Figure S1, Supporting Information). The reduced J_0 *and* n values indicate the decrease of leakage current and better defect passivation. The corresponding c-AFM images (Figure 2b,c) reveal significant reduction of current density, particularly in vicinity of GBs, confirming that the major reduction in J_0 originates from GBs. A higher Br content leads to a lower J_0, indicating reduced carrier recombination.

A detailed analysis on c-AFM current distribution at GBs and GIs provides a better understanding of the origins of reduced J_0. The average current in GIs decreases from 4.7 to 2.9 and to 1.8 nA, when Br concentration increases from 0 to 0.06 and to 0.16. For the same samples, the average current near GBs shows a more pronounced decrease from 12.7 to 9.3, and to 3.8 nA, indicating the passivation effect of the GBs by incorporating Br (Figure S3, Supporting Information). When Br concentration is increased to 0.06, high contrast particles (i.e., less conductive) at GBs start to appear (Figure S4, Supporting Information). These resistive particles are speculated to be due to Br segregation at GBs. To confirm this speculation, we conducted energy dispersive spectroscopy (EDS) measurement by scanning the e-beam along lines in representative GIs and at GBs (Figure S5, Supporting Information). The results show higher Br concentration at GBs than in GIs, confirming that Br segregation at GBs helps to passivate the defects and reduce conductivity. In particular, the brighter particles at GBs contain more Br content than the grains (Figure S6, Supporting Information).

The passivation effect of Br incorporation is confirmed by Kelvin probe force microscopy (KPFM) measurements. Figure 2d–f shows the KPFM maps of mixed Sn–Pb perovskites with various Br concentrations. For the Sn/Pb-0.00Br

Table 1. Summary of device performance metrics of our champion low-E_g Sn/Pb-0.06Br and Sn/Pb-0.00Br PSCs measured with AM1.5G 100 mW cm^{-2} illumination under reverse and forward direction voltage scans.

Cells		V_{OC} [V]	J_{SC} [mA cm^{-2}]	FF [%]	PCE [%]	R_S Ω cm^2]	R_{SH} [Ω cm^2]
Sn/Pb-0.06Br	Reverse	0.888	28.74	74.5	19.01	4.4	732.8
	Forward	0.888	28.72	74.6	19.03	4.3	733.6
Sn/Pb-0.00Br	Reverse	0.848	28.91	68.9	16.89	5.2	556.3
	Forward	0.847	28.92	69.5	17.03	5.1	555.5

© 2018 WILEY-VCH Verlag GmbH & Co. KGaA, Weinheim

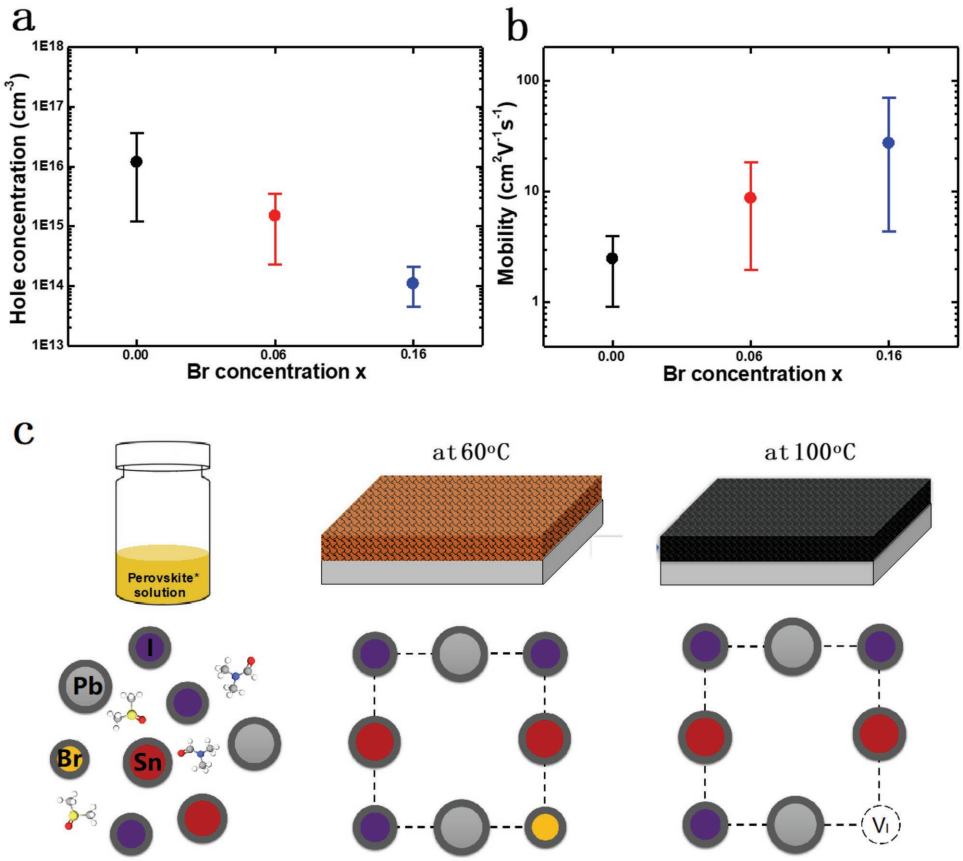

Figure 3. a) Hole concentration versus Br doping concentration and b) hole mobility versus Br doping concentration, of Sn/Pb-*x*Br films with $x = 0$, 0.06, and 0.16. c) Schematic diagram of Br-doping mechanisms.

perovskite film, the potential image exhibits lower potentials at GBs than GIs (Figure 2d). It is more evident in the line profile shown in Figure S7 (Supporting Information). The KPFM map reveals that the GBs contain a higher density of negatively charged defects than GIs. Upon Br-incorporation, the potential contrast between GB and GI is reduced (Figure 2e,f), indicating reduced density of negatively charged defects at GBs. A higher Br concentration correlates with a lower GB/GI potential contrast (Figure S7k,l, Supporting Information). Therefore, the KPFM results confirm that Br segregation passivates defects at GBs. Meanwhile, time-resolved photoluminescence (TRPL) decays also exhibit longer mean carrier lifetime (≈228 ns) for Sn/Pb-0.06Br perovskite film than that (≈98 ns) for Sn/Pb-0.00Br perovskite film, as shown in Figure S8 (Supporting Information).

Br incorporation not only passivates GBs, but also helps grain growth and improves crystallinity. As seen in the scanning electron microscopy (SEM) images (Figure S4, Supporting Information), the average grain size first increases as Br concentration increases, and then saturates at the Br concentration higher than 0.06. X-ray diffraction (XRD) patterns of all Sn/Pb-*x*Br perovskite films show strong (110) and (220) reflection peaks (Figure S9a, Supporting Information), indicating a preferred film orientation. Note that the Sn/Pb-0.06Br perovskite film exhibits the highest peak intensity and the narrowest full-width at half-maximum, compared with other Br-incorporated Sn/Pb films (Figure S9b, Supporting Information), which indicates the highest crystallinity. XRD patterns show no peaks from impurity phases, suggesting that Br incorporation forms single-phase mixed Sn/Pb perovskites. Moreover, the (110) peak at $2\theta = \approx 14°$ gradually shifts from 14.01° to 14.19° as the Br concentration increases (Figure S9c,d, Supporting Information), revealing the substitution of I by Br that reduces the perovskite lattice constant.

To evaluate the effects of Br incorporation on electrical properties of low-E_g Sn/Pb perovskites, we have performed Hall Effect measurements on Sn/Pb-*x*Br samples with $x = 0$, 0.06, and 0.16. As shown in **Figure 3**a, the average hole concentration of Sn/Pb-0.00Br film is measured to be $(1.18 \pm 1.12) \times 10^{16}$ cm^{-3}, which is much higher than that of medium-E_g perovskites. The high hole density is mainly attributed to the easy oxidation of Sn^{2+} to Sn^{4+}, which facilitates the formation of Sn vacancies (shallow acceptors). For Sn/Pb-0.06Br film, the hole density decreases to $(1.50 \pm 1.23) \times 10^{15}$ cm^{-3}, a reduction by one order of magnitude. The hole density of the Sn/Pb-0.16Br film further decreases to $(1.09 \pm 0.45) \times 10^{14}$ cm^{-3}. The reduced hole density leads to increased hole mobilities, $\mu = 2.5 \pm 1.0$ cm^2 V^{-1} s^{-1} for Sn/Pb-0.00Br film, $\mu = 8.7 \pm 6.1$ cm^2 V^{-1} s^{-1} for Sn/Pb-0.06Br film, and $\mu = 27.3 \pm 23.4$ cm^2 V^{-1} s^{-1} for Sn/Pb-0.16Br film (Figure 3b), due to reduced carrier scattering.

We speculate the following mechanism for the reduction in hole density by Br incorporation (Figure 3c): At the first

 © 2018 WILEY-VCH Verlag GmbH & Co. KGaA, Weinheim

annealing step at 60 °C, the precursor films are gradually converted into perovskite phase consisting of homogeneous intermixing of Br and I in the lattice of Sn–Pb perovskites. During the second annealing step at 100 °C, the relatively higher temperature drives Br atoms out of the perovskite crystal lattice, which subsequently segregate to GBs, as shown in the SEM and EDS results (Figures S4–S6, Supporting Information). Because Br has a higher partial vapor pressure than I, Br could escape from the perovskite lattice more easily than I, facilitating the formation of halide vacancies. For a halide vacancy, the defect state is formed by the dangling bonds of the neighboring divalent metal atoms (Pb and Sn).[35] Since the conduction band minimum (CBM) of the mixed Sn–Pb perovskite is mainly derived from the inactive Pb p orbital,[36] the halide vacancy levels are expected to be close to the CBM, which are shallow donors.[37] These shallow donors effectively compensate holes generated by Sn vacancies, leading to reduced hole density.

It has been reported that incorporating too high concentration of Br in iodide-based perovskites can lead to light-induced phase separation.[16,38] Such phase separation results in the formation of high density of defects, which is reflected by the high E_u. A larger E_u value is detrimental to device performance, in particular to V_{OC} and FF. To evaluate the effect of Br incorporation on the film quality and electronic disorder in the mixed Sn–Pb perovskite films, we have performed photothermal deflection spectroscopy (PDS) measurements (Figure S10, Supporting Information) to determine the E_u values[39–42] of our Br-incorporated mixed Sn/Pb perovskite films. The Sn/Pb-0.00Br film has the lowest E_u of 24.0 ± 0.8 meV. As the Br concentration increases, the E_u does not change much (24.1 ± 0.9 meV for $x = 0.04$ and 25.7 ± 0.6 meV for $x = 0.06$) at low Br concentrations. However, higher Br concentration reduces the electronic quality of the films, leading to the increase of the E_u to 29 ± 0.6 and 28 ± 0.5 meV for $x = 0.08$ and $x = 0.16$, respectively.

The above characterizations have shown mixed effects of Br incorporation on the performance of low-E_g PSCs. On one hand, Br incorporation reduces J_0, which is beneficial for V_{OC} and FF. On the other hand, Br incorporation reduces the hole density, which is not expected for solar cell performance. Furthermore, Br incorporation increases E_g, too much of which increases E_u values. Therefore, the Br concentration must be optimized to maximize the PCEs of low-E_g mixed Sn–Pb PSCs. To this end, we have fabricated a large number of low-E_g mixed Sn/Pb PSCs with various Br concentrations. The statistics of V_{OC}, J_{SC}, FF, and PCE of these PSCs are shown in **Figure 4**a–d and Table S1 (Supporting Information). The E_g obtained from spectroscopic ellipsometry measurements and absorbance spectra (Figure S11, Supporting Information) and average V_{OC} of PSCs with various Br concentrations are shown in Figure 4e and the dependence of V_{OC} deficit on Br concentrations is shown in Figure 4f and Table S2 (Supporting Information). The effects of Br incorporation are very clear. As the Br concentration increases, the average V_{OC} first increases and then saturates at $x = 0.06$, even though the E_g increases and J_0 decreases with higher Br concentration. This could be attributed to the significantly reduced hole densities and the large E_u values at high Br concentrations. The J_{SC} decreases with the increase of Br concentration, which can be explained by the increase of E_g. The FF first increases and reaches maximum at $x = 0.06$, and then decreases. The decrease in FF at higher Br concentration may be attributed to the significantly reduced hole densities and the large E_u values at high Br concentrations. As a result, the PCE also reaches the maximum at $x = 0.06$, exhibiting an average PCE of 18.75% with an average V_{OC} of 0.882 V, an average J_{SC} of 28.57 mA cm^{-2}, and an average FF of 74.4%. The lowest V_{OC} deficit achieved is 0.384 V at $x = 0.06$.

Figure 5a shows the J–V curves of a Sn/Pb-0.00Br cell and a Sn/Pb-0.06Br cell under a 100 mW cm^{-2} AM1.5G solar irradiation under forward voltage scan. The Sn/Pb-0.0Br cell has a PCE of 17.03% with a V_{OC} of 0.847 V, a J_{SC} of 28.92 mA cm^{-2}, and a FF of 69.5%, while the Sn/Pb-0.06Br cell has a PCE of 18.53% with a V_{OC} of 0.881 V, a J_{SC} of 28.51 mA cm^{-2}, and a FF of 73.8%, exhibiting increased V_{OC}, FF, and PCE. The external quantum efficiency (EQE) spectra (Figure S12, Supporting Information) show a spectral response to around 1040 nm for the Sn/Pb-0.00Br cell and a slightly blue shift for the Sn/Pb-0.06Br cell, primarily due to the increase in bandgap upon Br doping. The EQE-integrated J_{SC}s for the Sn/Pb-0.00Br and Sn/Pb-0.06Br cells are 28.3 and 28.1 mA cm^{-2}, respectively, in good agreement with the J_{SC} values from the J–V measurements.

To further evaluate the charge extraction/recombination processes in these solar cells, we perform light-intensity-dependence J–V measurements on Sn/Pb-0.00Br and Sn/Pb-0.06Br low-E_g PSCs. Figure S13 (Supporting Information) shows the power law dependence of the J_{SC} on light intensity ($J \propto I^{\alpha}$). The α values of 0.947 and 0.948 for Sn/Pb-0.00Br and Sn/Pb-0.06Br cells, respectively, are close to unity, suggesting a large energy barrier does not occur without space charge limited current during the charge extraction process.[43,44] As shown in Figure 5b, the V_{OC} increases monotonically with logarithmic light intensity, indicating that trap-assisted Shockley–Read–Hall recombination dominates in these devices. The Sn/Pb-0.06Br cell has a smaller ideality factor (1.24) than the Sn/Pb-0.00Br cell (1.46), consistent with the passivation of GBs by Br incorporation.

The J–V curves of our champion Sn/Pb-0.06Br PSC under a 100 mW cm^{-2} AM1.5G solar irradiation are shown in Figure 5c. The Sn/Pb-0.06Br cell achieves a PCE of 19.03 (19.01)% with a V_{oc} of 0.888 (0.888) V, a J_{sc} of 28.72 (28.74) mA cm^{-2}, and a FF of 74.6 (74.5)% when measured under forward (reverse) voltage scan, exhibiting a negligible degree of J–V hysteresis, as tabulated in Table 1. The steady-state efficiency is 18.5% by tracking the maximum output power under a 100 mW cm^{-2} AM1.5G solar irradiation (Figure 5d). To the best of our knowledge, the champion PCE of 19.03% is the highest value for low-E_g PSCs (≈1.1–1.3 eV) ever reported. The integrated J_{SC} over the AM 1.5G solar spectrum for Sn/Pb-0.06Br cell is 28.11 mA cm^{-2} (inset of Figure 5d), in good agreement with the J_{SC} from the J–V characterizations. We have fabricated 20 Sn/Pb-0.06Br devices in several batches. The PCE histogram (Figure S14, Supporting Information) suggests good reproducibility of our cells.

In summary, we have found that the high J_0 is one major cause for the unsatisfactory performance of low-E_g PSCs and have identified that the high J_0 is mainly attributed to the GBs. We further found that Br incorporation can effectively passivate GBs, leading to the reduction in J_0 by two to three orders of magnitude. As a result, the low-E_g PSCs have achieved the V_{OC} deficits as low as 0.384 V and FFs as high as 75% without

© 2018 WILEY-VCH Verlag GmbH & Co. KGaA, Weinheim

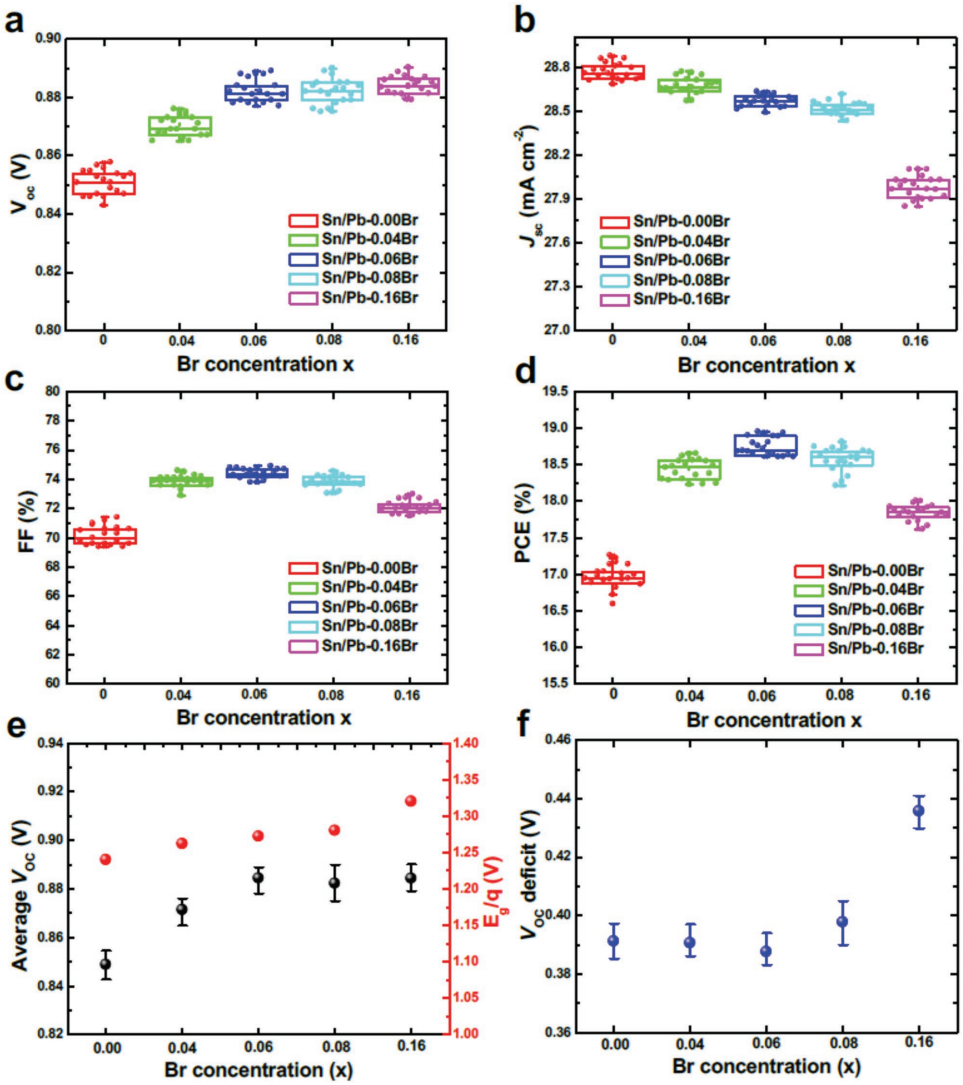

Figure 4. Statistics of all main photovoltaic parameters of Sn/Pb-*x*Br PSCs with *x* varying from 0 to 0.16 under a 100 mW cm^{-2} AM1.5G solar irradiation under forward voltage scan: a) V_{OC}, b) J_{SC}, c) FF, and d) PCE. 15–20 devices for Br concentration were fabricated and measured. e) Average V_{OC} versus Br concentration and E_g/q versus Br concentration. f) calculated V_{OC} deficit versus Br concentration.

obvious reduction in J_{SC}. The best-performing device achieved a PCE of >19%. Our work offers a promising potential to further improve the performance of low-E_g PSCs and all-perovskite tandem cells.

Experimental Section

Film Preparation: Pristine $(FASnI_3)_{0.6}(MAPbI_3)_{0.4}$ low-E_g perovskite precursor was prepared as reported in our previous works.[23,24] The details can be found below. The $FASnI_3$ precursor solution was prepared by dissolving 372 mg of SnI_2 and 172 mg of formamidinium iodide (FAI) (GreatCell Solar Company) with 10 mol% (15.6 mg) of SnF_2 in mixed N,N-dimethylmethanamide (DMF) (Sigma-Aldrich, anhydrous) and dimethyl sulfoxide (DMSO) (Sigma-Aldrich, anhydrous). The $MAPbI_3$ precursor solution was prepared by dissolving 461 mg PbI_2 and 159 mg methylammonium iodide (MAI) (GreatCell Solar Company) with 3.5 mol% (11.3 mg) lead thiocyanate ($Pb(SCN)_2$) (Sigma-Aldrich, 99.5%) dissolved in 630 µL DMF and 70 µL DMSO. The $(FASnI_3)_{0.6}(MAPbI_3)_{0.4}$ precursor solution was obtained by mixing stoichiometric amounts of $FASnI_3$ and $MAPbI_3$ perovskite precursor. The mixed solutions were kept for 30 min before spin-coating. $MAPbBr_3$ precursor solution was prepared by dissolving 367 mg $PbBr_2$ (Alfa Aesar) and 112 mg (MAI) in mixed solvent of 630 µL DMF and 70 µL DMSO. After being fully dissolved, a varying amount (*x*) of $MAPbBr_3$ solution was mixed with stoichiometric amount of $FASnI_3$ and $MAPbI_3$ to form $(FASnI_3)_{0.6}(MAPbI_3)_{0.4-x}(MAPbBr_3)_x$ (x = 0.00, 0.04, 0.06, 0.08, and 0.16) precursor solutions.

The samples for SEM and XRD measurements were obtained by spin-coating their corresponding precursor solutions onto ITO/PEDOT:PSS. The samples for PDS, spectroscopic ellipsometry (SE), unpolarized transmittance measurements were coated on glass.

Device Fabrication: The prepatterned ITO substrates were cleaned by ultrasonication in diluted Micro-90 detergent, deionized water, acetone, and isopropanol for 15 min, respectively. PEDOT:PSS films were coated on the cleaned ITO substrate at 4000 rpm for 50 s and then dried at 175 °C for 30 min. The precursors with varying Br concentration were spin-coated onto ITO/PEDOT:PSS at 5000 rpm for 60 s. Diethyl ether was applied drop-wise at 5 s onto the spinning substrate during the spin-coating. All perovskite films were annealed at 60 °C for 3 min and then 100°C for 7 min in a glove box. Finally, C_{60} (20 nm)/BCP (5 nm)/Ag (75 nm) were sequentially deposited by thermal evaporation to complete

 © 2018 WILEY-VCH Verlag GmbH & Co. KGaA, Weinheim

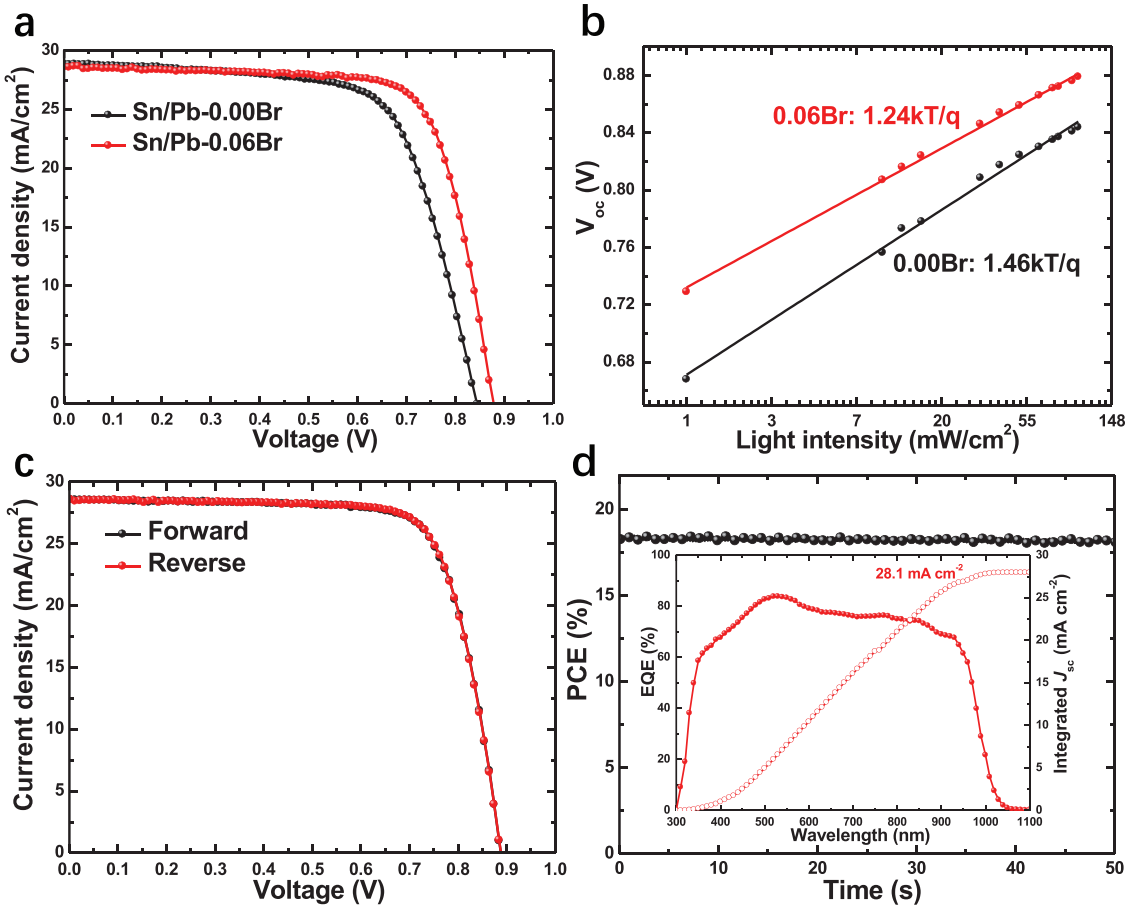

Figure 5. a) *J–V* curves of Sn/Pb-0.00Br and Sn/Pb-0.06Br cells under a 100 mW cm^{-2} AM1.5 G illumination measured under forward voltage scan. b) Light intensity-dependence of PSCs with Sn/Pb-0.00Br and Sn/Pb-0.06Br perovskite: V_{oc} versus light intensity. c) *J–V* curves and d) steady-state efficiency over time by tracking maximum power output, of our champion Sn/Pb-0.06Br cell measured under a 100 mW cm^{-2} AM1.5G illumination. Inset shows the EQE spectrum and its corresponding integrated J_{SC} over a 100 mW cm^{-2} AM1.5G solar spectrum.

the fabrication. The active areas of the devices were 0.12 cm^2. Devices were encapsulated with cover glass and UV-curable epoxy.

Film Characterization: High resolution field emission top-view SEM images of low-E_g perovskite films with varying Br concentration were taken with Hitachi S-4800. The crystal structure of low-E_g perovskite films with varying Br concentration was examined by XRD (RigakuUltima III) with Cu K_α radiation under operation conditions of 40 kV and 44 mA excitation. All layer thicknesses were determined using a Dektak surface profiler and calibrated by SE. The PDS measurements were collected using a custom system (PTS-3-PTD, Sciencetech Inc.) operating in transverse configuration[45] over a spectral range of 1400–800 nm (0.89–1.55 eV) in 10 nm steps. The monochromatic pump beam was modulated with a mechanical chopper at 0.2 Hz. The probe beam was a 633 nm laser of nominally 300 µm cross-sectional diameter. The full acquisition time for measurement of each film was ≈5 h. During PDS measurement, each film was immersed in a quartz cuvette containing a C_6F_{14} fluid (Fluorinert FC-72, Synquest Laboratories), which, in addition to being a thermally sensitive medium suitable for PDS measurement, also effectively eliminates atmospheric exposure of the perovskite films during measurement. Pristine films with varying Br concentration were prepared and subsequently immersed in C_6F_{14} with the transfer taking place in a pure N_2 environment. Thus, PDS measurements were collected for perovskite films without exposure to atmosphere. Immediately following PDS measurement, each film was removed from the C_6F_{14} fluid into the laboratory ambient for SE and unpolarized transmittance measurements. Both of these measurements were collected using a multichannel rotating-compensator SE[46,47] (M-2000FI, J. A. Woollam Co., Inc.) over a spectral range of 1676–210 nm (0.74–5.89 eV). The SE and unpolarized transmittance measurements were collected at 70° and 0° angles of incidence, respectively, with the SE being measured in terms of $N = \cos(2\psi)$, $C = \sin(2\psi)\cos\Delta$, and $S = \sin(2\psi)\sin\Delta$. The combined time for sample mounting, alignment, and data acquisition for these two measurements, i.e., the length of time the films were in atmosphere, was ≈5 min. Scanning probe microscopy techniques, c-AFM and KPFM, were performed on a Vecco D5000 AFM system in Ar glovebox equipped with a Nanoscope V controller. Both c-AFM and KPFM measurements used nanosensor point probe plus electrostatic force microscopy (PPP-EFM) tip for the scans; and one tip was used for each characterization method. The scans were on three different locations for every sample, and the results were similar. After scanning all samples, the first sample was rescanned to confirm there was no change of the tip. The scan area was 2 × 2 µm^2 with 1024 points on slow-axis and 256 lines on fast-axis. The scan rate was 0.2 hz per line. The c-AFM results were collected in contact mode. A bias voltage of 0.5 V was applied to the sample and the tip was grounded, the setup of which was similar to the dark current measurement. KPFM results were acquired in tapping mode. KPFM measured electrostatic potential on the sample surface with a spatial resolution of ≈30 nm and a potential resolution of ≈10 mV. TRPL measurements were conducted using a time correlated single photon counting module (Becker &Hickel Simple Tau SPCM 130-E/M module). Samples were excited by a 532 nm pulsed laser (Fianium model SC400-2, ≈5 ps pulse width, ≈150 µm spot diameter) at ≈10^{11} photons per pulse cm^{-2}. Radiative recombination events were detected via an InP/InGaAsP NIR PMT detector (Hamamatsu H10330A-45) after dispersion by an iHR-320 monochromator (900 g mm^{-1},

 © 2018 WILEY-VCH Verlag GmbH & Co. KGaA, Weinheim

850 nm blaze) grating. PL decay curves were biexponential in nature and fitted by iterative reconvolution with the measured system response function. Mean photogenerated carrier lifetimes for the biexponential fit were calculated by the weighted average method. Carrier concentration and mobility were measured using a Hall measurement controller (MMR technologies, H-50) and a benchtop electromagnet with a magnetic field of 0.26 T. Mixed Sn–Pb perovskite films were deposited onto glass substrates coated with patterned Au electrodes in a Van der Pauw configuration. The films were encapsulated with cover glass using UV-adhesive in a nitrogen-filled glove box and taken out to perform the Hall measurement in air. The Au contacts outside the encapsulation area were connected to the Hall controller. The film thickness of ≈620 nm was determined by cross-sectional SEM and used to calculate the carrier concentration and mobility. For each Br concentration, 6 samples were measured, and the statistic results were calculated.

Device Characterization: J–V curves were measured in air under 100 mW cm^{-2} AM1.5G solar irradiation (PV Measurements Inc.) with a Keithley 2400 Source Meter. The light intensity for *J–V* measurements was calibrated by a standard silicon wafer solar cell and the perovskite solar cells were certified by Newport. Light intensity dependence measurements were made by decreasing the solar irradiation with neutral density light filters. The steady-state efficiencies were obtained by tracking the maximum power point. All characterizations and measurements were performed in ambient. The cells with an active area of 0.11 cm^2 as defined by the mask were measured. EQE spectra were performed from 300 to 1150 nm on a QE system (PV Measurements Inc., model IVQE8-C QE system without bias voltage). A standard silicon wafer cell was used as the reference for the EQE measurement.

Supporting Information

Supporting Information is available from the Wiley Online Library or from the author.

Acknowledgements

C.L. and Z.S. contributed equally to this work. This work was financially supported by the U.S. Department of Energy (DOE) SunShot Initiative under the Next Generation Photovoltaics 3 program (Grant No. DE-FOA-0000990) for device fabrication, the Office of Naval Research under Contract no. N00014-17-1-2223 for device characterization, Air Force Research Laboratory under Space Vehicles Directorate (Grant No. FA9453-11-C-0253) for material synthesis, and the Ohio Research Scholar Program for device modeling. The work at the National Renewable Energy Laboratory was supported by the U.S. Department of Energy SunShot Initiative under the Next Generation Photovoltaics 3 program (Grant No. DE-FOA-0000990) and under Contract No. DE-AC36-08-GO28308 with Alliance for Sustainable Energy, LLC, the Manager and Operator of the National Renewable Energy Laboratory.

Conflict of Interest

The authors declare no conflict of interest.

Keywords

dark saturation current, grain boundary passivation, low-bandgap perovskites, perovskite solar cells

Received: October 9, 2018
Revised: November 14, 2018
Published online:

[1] H. Tan, A. Jain, O. Voznyy, X. Lan, F. P. García de Arquer, J. Z. Fan, R. Quintero-Bermudez, M. Yuan, B. Zhang, Y. Zhao, F. Fan, P. Li, L. N. Quan, Y. Zhao, Z.-H. Lu, Z. Yang, S. Hoogland, E. H. Sargent, *Science* **2017**, *355*, 722.
[2] S. S. Shin, E. J. Yeom, W. S. Yang, S. Hur, M. G. Kim, J. Im, J. Seo, J. H. Noh, S. I. Seok, *Science* **2017**, *356*, 167.
[3] J. Huang, Y. Yuan, Y. Shao, Y. Yan, *Nat. Rev. Mater.* **2017**, *2*, 17042.
[4] Y. Wu, X. Yang, W. Chen, Y. Yue, M. Cai, F. Xie, E. Bi, A. Islam, L. Han, *Nat. Energy* **2016**, *1*, 16148.
[5] Z. Song, C. L. McElvany, A. B. Phillips, I. Celik, P. W. Krantz, S. C. Watthage, G. K. Liyanage, D. Apul, M. J. Heben, *Energy Environ. Sci.* **2017**, *10*, 1297.
[6] D. Zhao, C. Wang, Z. Song, Y. Yu, C. Chen, X. Zhao, K. Zhu, Y. Yan, *ACS Energy Lett.* **2018**, *3*, 305.
[7] A. Kojima, K. Teshima, Y. Shirai, T. Miyasaka, *J. Am. Chem. Soc.* **2009**, *131*, 6050.
[8] H.-S. Kim, C.-R. Lee, J.-H. Im, K.-B. Lee, T. Moehl, A. Marchioro, S.-J. Moon, R. Humphry-Baker, J.-H. Yum, J. E. Moser, M. Gratzel, N.-G. Park, *Sci. Rep.* **2012**, *2*, 591.
[9] NREL, Research Cell Record Efficiency Chart, https://www.nrel.gov/pv/assets/pdfs/pv-efficiencies-07-17-2018.pdf (accessed: October 2018).
[10] J. J. Berry, J. van de Lagemaat, M. M. Al-Jassim, S. Kurtz, Y. Yan, K. Zhu, *ACS Energy Lett.* **2017**, *2*, 2540.
[11] G. E. Eperon, T. Leijtens, K. A. Bush, R. Prasanna, T. Green, J. T.-W. Wang, D. P. McMeekin, G. Volonakis, R. L. Milot, R. May, A. Palmstrom, D. J. Slotcavage, R. A. Belisle, J. B. Patel, E. S. Parrott, R. J. Sutton, W. Ma, F. Moghadam, B. Conings, A. Babayigit, H.-G. Boyen, S. Bent, F. Giustino, L. M. Herz, M. B. Johnston, M. D. McGehee, H. J. Snaith, *Science* **2016**, *354*, 861.
[12] M. Anaya, G. Lozano, M. E. Calvo, H. Míguez, *Joule* **2017**, *1*, 769.
[13] T. Leijtens, K. A. Bush, R. Prasanna, M. D. McGehee, *Nat. Energy* **2018**, *1*, 11.
[14] G. E. Eperon, M. T. Hörantner, H. J. Snaith, *Nat. Rev. Chem.* **2017**, *1*, 0095.
[15] K. Ghimire, D. Zhao, Y. Yan, N. J. Podraza, *AIP Adv.* **2017**, *7*, 075108.
[16] D. P. McMeekin, G. Sadoughi, W. Rehman, G. E. Eperon, M. Saliba, M. T. Hörantner, A. Haghighirad, N. Sakai, L. Korte, B. Rech, M. B. Johnston, L. M. Herz, H. J. Snaith, *Science* **2016**, *351*, 151.
[17] Y. Yu, C. Wang, C. R. Grice, N. Shrestha, D. Zhao, W. Liao, L. Guan, R. A. Awni, W. Meng, A. J. Cimaroli, K. Zhu, R. J. Ellingson, Y. Yan, *ACS Energy Lett.* **2017**, *2*, 1177.
[18] H. Tan, F. Che, M. Wei, Y. Zhao, M. I. Saidaminov, P. Todorović, D. Broberg, G. Walters, F. Tan, T. Zhuang, B. Sun, Z. Liang, H. Yuan, E. Fron, J. Kim, Z. Yang, O. Voznyy, M. Asta, E. H. Sargent, *Nat. Commun.* **2018**, *9*, 3100.
[19] Y. Lin, B. Chen, F. Zhao, X. Zheng, Y. Deng, Y. Shao, Y. Fang, Y. Bai, C. Wang, J. Huang, *Adv. Mater.* **2017**, *29*, 1700607.
[20] F. Hao, C. C. Stoumpos, R. P. H. Chang, M. G. Kanatzidis, *J. Am. Chem. Soc.* **2014**, *136*, 8094.
[21] R. Prasanna, A. Gold-Parker, T. Leijtens, B. Conings, A. Babayigit, H.-G. Boyen, M. F. Toney, M. D. McGehee, *J. Am. Chem. Soc.* **2017**, *139*, 11117.
[22] A. Rajagopal, Z. Yang, S. B. Jo, I. L. Braly, P.-W. Liang, H. W. Hillhouse, A. K. Y. Jen, *Adv. Mater.* **2017**, *29*, 1702140.
[23] W. Liao, D. Zhao, Y. Yu, N. Shrestha, K. Ghimire, C. R. Grice, C. Wang, Y. Xiao, A. J. Cimaroli, R. J. Ellingson, N. J. Podraza, K. Zhu, R.-G. Xiong, Y. Yan, *J. Am. Chem. Soc.* **2016**, *138*, 12360.
[24] D. Zhao, Y. Yu, C. Wang, W. Liao, N. Shrestha, C. R. Grice, A. J. Cimaroli, L. Guan, R. J. Ellingson, K. Zhu, X. Zhao, R.-G. Xiong, Y. Yan, *Nat. Energy* **2017**, *2*, 17018.
[25] S. Shao, Y. Cui, H. Duim, X. Qiu, J. Dong, G. H. ten Brink, G. Portale, R. C. Chiechi, S. Zhang, J. Hou, M. A. Loi, *Adv. Mater.* **2018**, *30*, 1803703.
[26] Z. Yang, A. Rajagopal, A. K.-Y. Jen, *Adv. Mater.* **2017**, *29*, 1704418.

 © 2018 WILEY-VCH Verlag GmbH & Co. KGaA, Weinheim

[27] Y. Zong, N. Wang, L. Zhang, M.-G. Ju, X. C. Zeng, X. W. Sun, Y. Zhou, N. P. Padture, *Angew. Chem., Int. Ed.* **2017**, *56*, 12658.
[28] G. Kapil, T. S. Ripolles, K. Hamada, Y. Ogomi, T. Bessho, T. Kinoshita, J. Chantana, K. Yoshino, Q. Shen, T. Toyoda, T. Minemoto, T. N. Murakami, H. Segawa, S. Hayase, *Nano Lett.* **2018**, *18*, 3600.
[29] D. Zhao, C. Chen, C. Wang, M. M. Junda, Z. Song, C. R. Grice, Y. Yu, C. Li, B. Subedi, N. J. Podraza, X. Zhao, G. Fang, R.-G. Xiong, K. Zhu, Y. Yan, *Nat. Energy* **2018**, https://doi.org/10.1038/s41560-018-0278-x.
[30] P. Singh, N. M. Ravindra, *Sol. Energy Mater. Sol. Cells* **2012**, *101*, 36.
[31] C. Wang, C. Xiao, Y. Yu, D. Zhao, R. A. Awni, C. R. Grice, K. Ghimire, D. Constantinou, W. Liao, A. J. Cimaroli, P. Liu, J. Chen, N. J. Podraza, C.-S. Jiang, M. M. Al-Jassim, X. Zhao, Y. Yan, *Adv. Energy Mater.* **2017**, *7*, 17000414.
[32] C. Wang, D. Zhao, C. R. Grice, W. Liao, Y. Yu, A. Cimaroli, N. Shrestha, P. J. Roland, J. Chen, Z. Yu, P. Liu, N. Cheng, R. J. Ellingson, X. Zhao, Y. Yan, *J. Mater. Chem. A* **2016**, *4*, 12080.
[33] C. Wang, D. Zhao, Y. Yu, N. Shrestha, C. R. Grice, W. Liao, A. J. Cimaroli, J. Chen, R. J. Ellingson, X. Zhao, Y. Yan, *Nano Energy* **2017**, *35*, 223.
[34] W. Liao, D. Zhao, Y. Yu, C. R. Grice, C. Wang, A. J. Cimaroli, P. Schulz, W. Meng, K. Zhu, R.-G. Xiong, Y. Yan, *Adv. Mater.* **2016**, *28*, 9333.
[35] W.-J. Yin, T. Shi, Y. Yan, *J. Phys. Chem. C* **2015**, *119*, 5253.
[36] A. Goyal, S. McKechnie, D. Pashov, W. Tumas, M. v. Schilfgaarde, V. Stevanović, *Chem. Mater.* **2018**, *30*, 3920.
[37] W.-J. Yin, T. Shi, Y. Yan, *Appl. Phys. Lett.* **2014**, *104*, 063903.
[38] J. Cao, S. X. Tao, P. A. Bobbert, C.-P. Wong, N. Zhao, *Adv. Mater.* **2018**, *30*, 1707350.
[39] A. Sadhanala, F. Deschler, T. H. Thomas, S. E. Dutton, K. C. Goedel, F. C. Hanusch, M. L. Lai, U. Steiner, T. Bein, P. Docampo, D. Cahen, R. H. Friend, *J. Phys. Chem. Lett.* **2014**, *5*, 2501.
[40] S. De Wolf, J. Holovsky, S.-J. Moon, P. Löper, B. Niesen, M. Ledinsky, F.-J. Haug, J.-H. Yum, C. Ballif, *J. Phys. Chem. Lett.* **2014**, *5*, 1035.
[41] S. Pathak, A. Sepe, A. Sadhanala, F. Deschler, A. Haghighirad, N. Sakai, K. C. Goedel, S. D. Stranks, N. Noel, M. Price, S. Hüttner, N. A. Hawkins, R. H. Friend, U. Steiner, H. J. Snaith, *ACS Nano* **2015**, *9*, 2311.
[42] B. Zhao, M. Abdi-Jalebi, M. Tabachnyk, H. Glass, V. S. Kamboj, W. A. Nie, J. Pearson, Y. Puttisong, K. C. Gödel, H. E. Beere, D. A. Ritchie, A. D. Mohite, S. E. Dutton, R. H. Friend, A. Sadhanala, *Adv. Mater.* **2017**, *29*, 1604744.
[43] D. Zhao, W. Ke, C. R. Grice, A. J. Cimaroli, X. Tan, M. Yang, R. W. Collins, H. Zhang, K. Zhu, Y. Yan, *Nano Energy* **2016**, *19*, 88.
[44] D. Zhao, M. Sexton, H.-Y. Park, G. Baure, J. C. Nino, F. So, *Adv. Energy Mater.* **2015**, *5*, 1401855.
[45] W. B. Jackson, N. M. Amer, A. C. Boccara, D. Fournier, *Appl. Opt.* **1981**, *20*, 1333.
[46] J. Lee, P. I. Rovira, I. An, R. W. Collins, *Rev. Sci. Instrum.* **1998**, *69*, 1800.
[47] B. Johs, J. A. Woollam, C. M. Herzinger, J. N. Hilfiker, R. A. Synowicki, C. L. Bungay, *SPIE Proc.* **1999**, *CR72*, 29.

© 2018 WILEY-VCH Verlag GmbH & Co. KGaA, Weinheim